Simplifying Electron Beam Channeling in Scanning Transmission Electron Microscopy (STEM)

Ryan J. Wu, Anudha Mittal, Michael L. Odlyzko, and K. Andre Mkhoyan[*]

Department of Chemical Engineering and Materials Science, University of Minnesota, Minneapolis, MN 55455, USA

Abstract: Sub-angstrom scanning transmission electron microscopy (STEM) allows quantitative column-by-column analysis of crystalline specimens via annular dark-field images. The intensity of electrons scattered from a particular location in an atomic column depends on the intensity of the electron probe at that location. Electron beam channeling causes oscillations in the STEM probe intensity during specimen propagation, which leads to differences in the beam intensity incident at different depths. Understanding the parameters that control this complex behavior is critical for interpreting experimental STEM results. In this work, theoretical analysis of the STEM probe intensity reveals that intensity oscillations during specimen propagation are regulated by changes in the beam's angular distribution. Three distinct regimes of channeling behavior are observed: the high-atomic-number (Z) regime, in which atomic scattering leads to significant angular redistribution of the beam; the low-Z regime, in which the probe's initial angular distribution controls intensity oscillations; and the intermediate-Z regime, in which the behavior is mixed. These contrasting regimes are shown to exist for a wide range of probe parameters. These results provide a new understanding of the occurrence and consequences of channeling phenomena and conditions under which their influence is strengthened or weakened by characteristics of the electron probe and sample.

Key words: STEM, multislice, channeling, Z-dependence

INTRODUCTION

Early studies examining the penetration of charged particles in crystalline materials showed that incident particles appear to propagate along the atomic columns of the crystal, a phenomenon referred to as channeling (Lindhard, 1965; Kreiner et al., 1970; Kambe et al., 1974; Komaki & Fujimoto, 1974; Tsyganov, 1976). More recent studies have focused on this channeling behavior for electron probes in conventional transmission electron microscopy (TEM) (Fertig & Rose, 1981; Pennycook, 1988; Sinkler & Marks, 1999; Van Aert et al., 2007) and scanning TEM (STEM) (Loane et al., 1988; Hillyard & Silcox, 1993, 1995; Hillyard et al., 1993; Nellist & Pennycook, 1999; Hovden et al., 2012) because it influences the quantitative interpretation of high-resolution images. Simulations of a STEM probe propagating along a column of atoms have shown oscillatory changes in the electron intensity along the column (Loane et al., 1988; Voyles et al., 2004). These depth-dependent intensity oscillations, considered channeling effects of the electron probe, change the intensity and angular distribution of incident electrons as a function of thickness. Thus, a quantitative interpretation of images and spectroscopy data obtained in STEM necessitates a careful understanding of channeling. These short-range oscillations along the atomic columns of crystals have become even more critical in aberration-corrected STEMs due to shorter depths of focus of the probe (Borisevich et al., 2006; D'Alfonso et al., 2007).

Simulation of electron beam propagation through the specimen of interest remains the most proven method for interpreting the effect of channeling in STEM. For example, STEM characterization of doped crystalline specimens has compared simulated annular dark-field (ADF)-STEM images, which are governed by beam channeling, to experimentally observed images, in order to identify dopant atoms and their three-dimensional (3D) locations (Voyles et al., 2003, 2004; Hwang et al., 2013; Ishikawa et al., 2014). Simulations have also shown that channeling effects allow determination of film thickness and the number of layers in ADF-STEM images (LeBeau et al., 2010; Wu et al., 2014; Odlyzko et al., 2016). Although these experimental studies exploited channeling effects to introduce a novel method of sample characterization using STEM, the channeling effects themselves are not explored thoroughly.

Theoretical studies of TEM and STEM image formation have used different models of beam propagation to account for channeling. For example, the "1S state" model of beam propagation treats intensity oscillations during channeling as oscillations of the probe wave function in a bound state localized along atomic columns (Op de Beeck & Van Dyck, 1996; Van Dyck & Op de Beeck, 1996), and Hovden et al. (2012) used a tight-binding approximation on two neighboring atomic columns to show that the overlap of adjacent orbitals can cause beam intensity oscillations between the columns during channeling, which can then lead to image artifacts. However, these works focus on rigorous treatments to model the beam propagation within materials for the purposes of image formation or interpretation; whereas, a less rigorous approach can provide a more accessible understanding of how channeling affects experimental results.

In this work, we attempt to go one step further in bridging the gap between theoretical models and experimental

application by simplifying the explanation of electron channeling along atomic columns and the roles of the crystal. Here, we focus primarily on the beam intensity oscillations along atomic columns and the parameters that govern them. Simulations are performed to study the intensity oscillations of the STEM probe that occur during its propagation through a crystalline sample. Beam intensity depth profiles are first simulated to visualize channeling effects and to justify the use of simpler isolated atomic columns as a model for later study. Subsequently, the origin of these intensity oscillations is discussed in terms of the fluctuation of intensity along an atomic column during and between scattering events within the column. Finally, the STEM probe parameters and sample characteristics are varied to explore the roles of the governing parameters.

METHODS

STEM probes and their propagation through specimens were simulated using the *multislice* method (Cowley & Moodie, 1957) with the TEMSIM code package (Kirkland, 2010), which has been demonstrated to be an excellent approach for understanding intricacies of quantitative ADF-STEM images of crystalline and crystalline/amorphous specimens (LeBeau et al., 2008, 2010; Mkhoyan et al., 2008; Kourkoutis et al., 2011), as well as those of convergent-beam electron diffraction patterns (Loane et al., 1991; Xu et al., 1991). All simulations, unless otherwise specified, were performed for a 100 keV STEM electron probe with a convergence angle of $\alpha_{obj} = 25$ mrad. Aberration-free STEM probes with $C_s = 0$ were used in these simulations for simplicity because small residual aberrations do not significantly influence the beam channeling behavior, as shown in Appendix A. Simulations were performed on 3.0×3.0 nm^2 supercells using $1,024 \times 1,024$ pixel^2 grids for transmission and probe functions. The atomic thermal displacements are not considered, unless otherwise specified, because a majority of simulations are performed on hypothetical isolated single atomic columns. It should be noted that incorporating atomic thermal displacement is necessary for a quantitative analysis of channeling, but for a conceptual understanding, as is the case here, it is not critical. Slice thickness was set to be 0.2 nm unless otherwise specified. In all cases, atomic columns are perfectly aligned with the microscope optical axis, and the probe was centered at the top of the column of interest. The transverse planes in these simulations are in the x–y plane, and the positive z-axis is defined as the direction of beam propagation, as shown in Figure 1a. The normalization of beam intensity, which is slightly different than conventional TEMSIM normalization (Kirkland, 2010), is described in Appendix B.

RESULTS

Oscillations in Crystals

As the STEM probe channels differently depending on the material (Hillyard & Silcox, 1993, 1995; Hillyard et al., 1993;
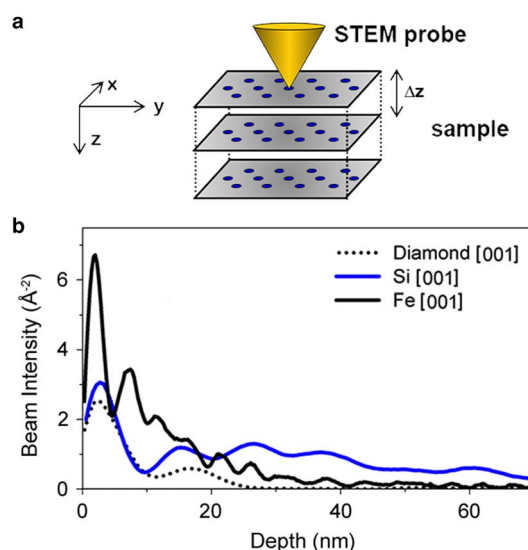

Figure 1. a: Schematic diagram of a STEM probe and sliced specimen along with coordinate axes used in these simulations. **b:** Beam intensity profiles of a STEM probe channeling through an atomic column in diamond, Si, and α-Fe oriented along the [001] crystal axis.

Yu & Silcox, 2004; Haruta et al., 2009; Mittal & Mkhoyan, 2011), it is essential to start by comparing the probe propagation behavior in various crystals. Figure 1b shows a comparison of the beam intensities along the optic axis during beam propagation through three different crystalline materials: C (diamond allotrope), Si, and α-Fe, all oriented along the [001] crystallographic axis. These materials were selected to represent low-, intermediate-, and high-atomic-number (Z) specimens, respectively. The beam intensity oscillates with depth in all three cases. However, the details of the oscillation, such as the amplitude, frequency, and decay rate, vary from one crystal to another. This variation suggests that Z of the atoms is a key parameter governing channeling behavior. These same oscillations can be presented in two-dimensional (2D) depth profiles (x–z plots) as shown in Figure 2, where the spread of the beam off the optic axis can also be visualized. Simulation of the STEM probe propagating in vacuum without a specimen is included for comparison. In vacuum, the probe loses a majority of its intensity along the optic axis after propagating ~25 nm. This behavior is similar to that in C [001] (low-Z crystal), in which substantial intensity shifts away from the optic axis after propagating ~25 nm. However, the presence of atoms, or scattering centers, appears to trap some of the propagating beam in neighboring columns for ~20 nm before the beam continues to spread to the next neighboring columns. This is a stark contrast to Fe [001] (high-Z crystal), in which the beam remains on the original column as if the atomic column were isolated. Propagation in Si [001] shows a mixed behavior akin to both the low- and high-Z cases. These observations suggest two limiting regimes: at high Z, the behavior of a propagating beam along an atomic column in a crystal becomes similar to that for an identical column in isolation, and at low Z, the beam behaves similarly to that in vacuum, as if there is not a sample.

To test these limits, the same simulations were performed for Au and He crystals, which represent the limiting high- and low-Z cases, respectively, along with their corresponding isolated columns. Figure 3 compares the oscillations of the STEM probe intensity along the optic axis for the isolated atomic columns and the crystals. As can be seen in Figure 3a, by $Z_{Au} = 79$, an electron beam propagating along a crystal behaves nearly identical to an electron beam propagating along the corresponding isolated column. This agreement occurs at high Z when the attractive Coulomb potential of the atoms is strong enough to focus the majority of the electron beam along the original column where the probe was placed and away from neighboring columns. For the opposite limit, Figure 3b shows that an electron propagating along an He crystal ($Z_{He} = 2$) also behaves as if it were propagating along its corresponding isolated column, but more importantly, it also behaves as in vacuum without He. In this low-Z limit, neither the original column nor the neighboring columns can trap the beam due to their weak Coulombic attraction, and the beam simply propagates as if there were no atomic column or crystal. Overall, both of these limits allow beam propagation in low- and high-Z crystals to be approximated and studied as propagation in simpler isolated columns (Yu & Silcox, 2004). The validity of

this isolated column approximation was also demonstrated in a previous study (Van Dyck & Op de Beeck, 1996). However, it is important to note that these limits represent two competing mechanisms, and thus, the approximation cannot be used for beam propagation in intermediate-Z crystals.

Intensity Oscillations in High-Z Columns

Because beam propagation in high-Z crystals behaves nearly identical to that in their respective isolated columns, as discussed previously, simpler isolated atomic columns can be used instead to understand the origin of beam intensity oscillations within a column. To study the effect on beam propagation in high-Z crystals, first, a column of Ga atoms with an interatomic spacing of 0.5 nm is used, as shown Figure 4a. Ga ($Z_{Ga} = 31$) was chosen to represent considerably high-Z elements ($Z \gtrsim Z_{Fe} = 26$). The beam intensity of each slice along the Ga column is presented in Figure 4b. Although a slice thickness equal to the interatomic spacing ($\Delta z = 0.5$ nm) is sufficient to observe the oscillatory behavior of the beam, a finer slice thickness of $\Delta z = 0.1$ nm can be used to observe the behavior of the beam between scattering events. The jagged shape is a result of a sudden increase in
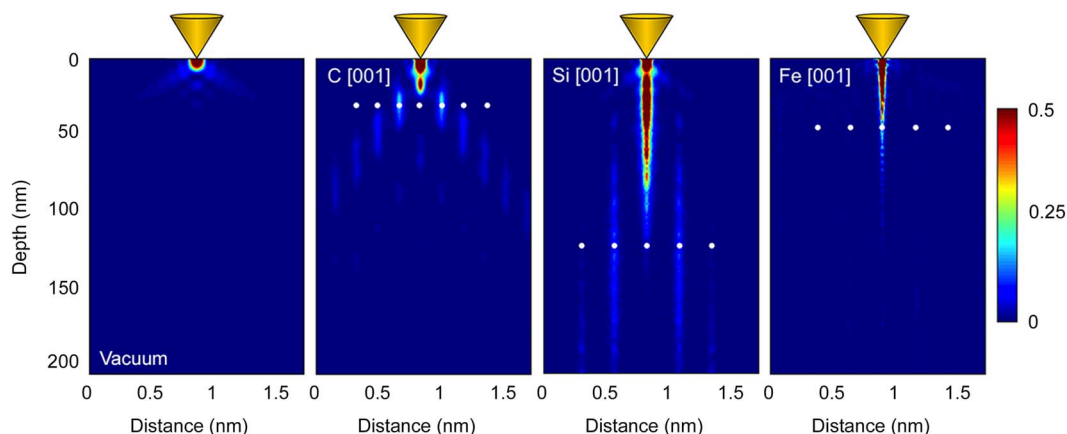

Figure 2. 2D beam intensity depth profiles of a simulated STEM probe propagating in vacuum, crystals of C [001] (diamond allotrope), Si [001], and α-Fe [001], where [001] denotes the crystallographic zone axis of beam propagation. The cross sections are along the [100] direction (x-axis) perpendicular to the incident beam direction (z-axis). The solid circles mark positions of atomic columns.
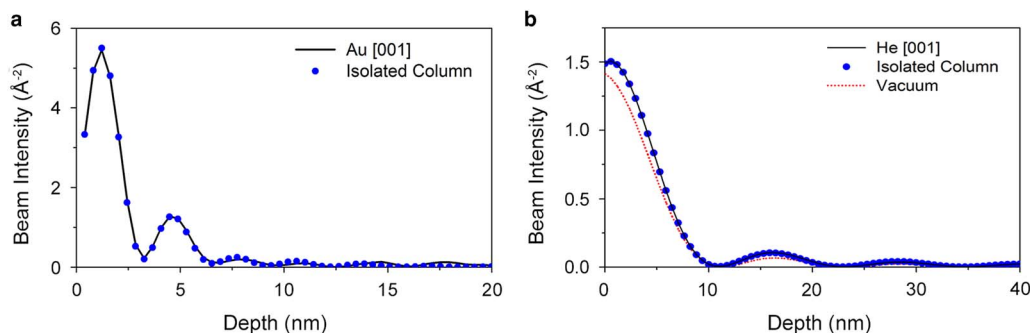

Figure 3. a: Comparison of beam intensity depth profiles for a STEM probe propagating along a [001]-oriented Au FCC crystal and in an isolated column of Au. **b:** Comparison of beam intensity for a STEM probe propagating along a [001]-oriented He HCP crystal, in an isolated column of He, and in vacuum without a specimen.
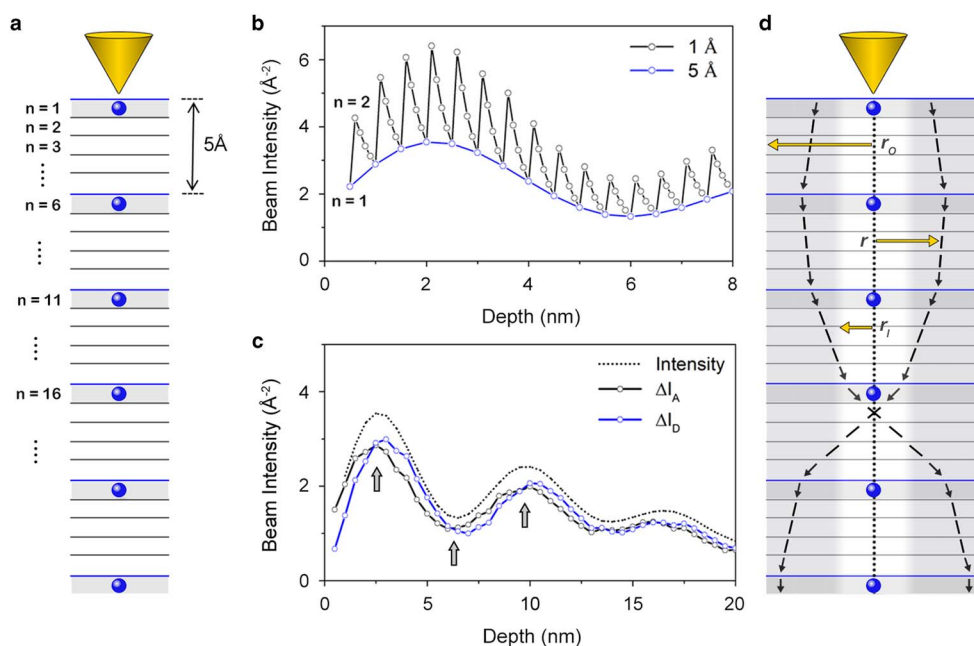
Figure 4. a: Schematic illustration of an isolated Ga column with interatomic spacing of 5 Å. Slicing with two different slice thicknesses, 1 Å and 5 Å, are shown. **b:** Beam intensity profile along this isolated atomic column simulated with slice thicknesses of 1 Å and 5 Å. **c:** Separated changes in accumulation, and dissipation. The arrows in (**c**) indicate the depths at which the inequality between and reverses. **d:** Schematic illustration of beam focusing and defocusing caused by atomic scattering as the beam propagates along the isolated column. The lines and arrows in (**d**) show the average positions and directions of two symmetric electrons at each slice.

intensity in one slice (0.1 nm) followed by a more gradual decrease over four slices (0.4 nm). Accumulation of beam intensity along the optic axis is observed immediately after each scattering event when the beam scatters off the Ga atom. If the intensity of the slice n is denoted as I_n, the intensity accumulation can be defined as $\Delta I_A = I_n - I_{n-1}$ for $n = 2, 7, 12\ldots$ (slices $n = 1, 6, 11\ldots$ are slices containing Ga). For all other slices, the beam is propagating in vacuum, and its intensity is dissipating. This dissipation can be defined similarly as $\Delta I_D = I_n - I_{n+4}$, the change in beam intensity over the next four slices before the next scattering event. Figure 4c shows both accumulation and dissipation as a function of depth as the beam propagates through the column. The inequality between the accumulation, ΔI_A, and dissipation, ΔI_D, describes the oscillations in beam intensity. As shown in Figure 4c, when $\Delta I_A > \Delta I_D$, the beam intensity along the atomic column rises, and, similarly, when $\Delta I_A < \Delta I_D$, the beam intensity falls. These two regions consequently can be denoted as "rise" and "fall," respectively. The electron beam alternates between these two regions as it propagates through the sample, an effect that ultimately manifests itself as intensity oscillations within individual columns. This accumulation and dissipation description of intensity oscillations is consistent with the "atomic lensing model" proposed in a recent study which superimposed the focusing effect of each individual atom in a column to describe nonlinear intensity increases (van den Bos et al., 2016). It should be noted that, whereas in real crystals, the intensity accumulation and dissipation occur continuously as the beam propagates through the sample, discretization in the *multislice* method

using slices is still a very accurate representation of beam propagation, as discussed in Appendix C.

The alternation between the rise and fall region, as described by the inequality between ΔI_A and ΔI_D is ultimately an effect of the attractive Coulomb interaction between the propagating electrons of the beam and the atomic nuclei of the column. As the electron probe propagates along the isolated column, each atom along the column scatters the probe, thereby changing the directions of individual electrons, as depicted in Figure 4d. The strength of the attractive Coulomb potential, and, hence, the effect of scattering depends on r, the distance between the average spatial distribution of the electron and the atoms in the column. At distances far from the column, r_o, the electrons are focused by atomic scattering because the attractive Coulomb interaction is small. Each scattering event changes the direction of the electrons slightly toward the atomic column, as shown in Figure 4d for the first three scattering events (at slices containing atoms). Thus, the intensity of the probe along the atomic column in this region accumulates rather than dissipates ($\Delta I_A > \Delta I_D$). When the average spatial distribution of electrons is below a critical distance, r_I, the attractive Coulomb interaction becomes large, and the scattering actually forces the electrons to defocus by "overshooting" the atoms. An exaggerated representation of the resulting probe moving away from the atomic column is depicted at the fourth scattering event in Figure 4d. As a result, the intensity of the probe dissipates along the atomic column ($\Delta I_D > \Delta I_A$) and continues to do so until subsequent scattering focuses the beam back again. This physical picture
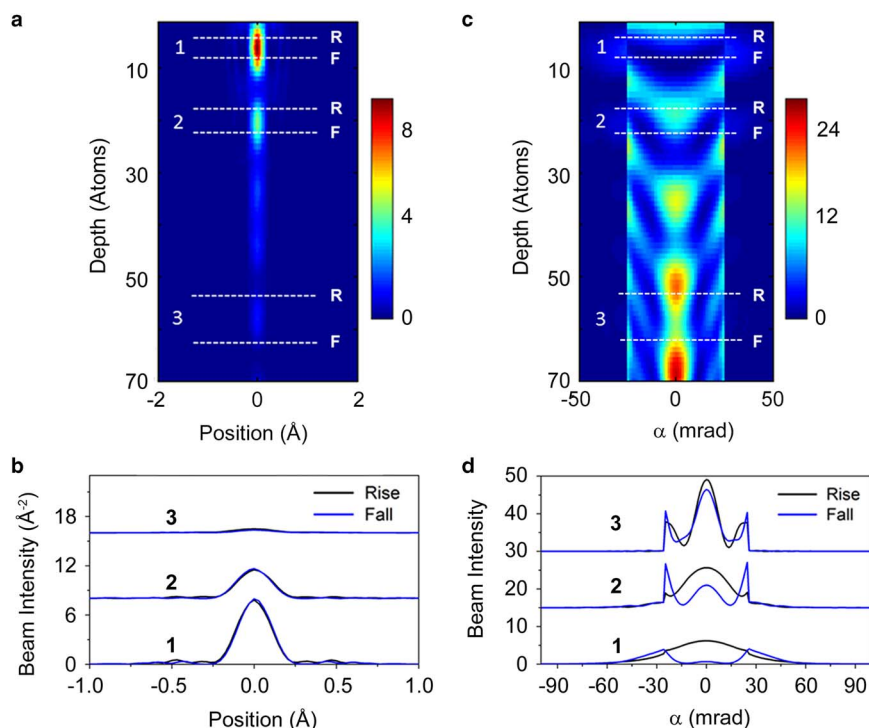
Figure 5. a: 2D beam intensity depth profile of a STEM probe propagating through an isolated Ga column with interatomic spacing of 2 Å. Depth locations of equal intensities along the "rise" and "fall" are indicated with dashed lines. **b:** Line scans of spatial distributions at different depths corresponding to pairs of position marked by dashed lines in (**a**). **c:** 2D beam intensity depth profile of the same STEM probe in reciprocal (or angular) space ($k = \alpha/\lambda$). **d:** Line scans of angular distributions corresponding to positions marked by dashed lines in (**c**).

suggests that scattering centers, depending on r, either focus ($\Delta I_A > \Delta I_D$) or defocus ($\Delta I_D > \Delta I_A$) the propagating probe.

The effect of atomic scattering on ΔI_A and ΔI_D can be further studied in an isolated column of Ga with an interatomic spacing of 0.2 nm as shown in Figure 5a, where the smaller interatomic spacing increases the rate of atomic scattering. Pairs of points with equal intensity along the optic axis are marked. Each point in a pair is along either the rise or fall regions of an intensity oscillation maximum and is consequently denoted as "R" or "F," respectively. The beam intensity lateral profiles for these marked points, which represent the spatial distributions of the beam, are shown in Figure 5b. For all three intensity oscillations shown, the spatial distribution of the beam is nearly identical between the rise and the fall. However, as noted previously, the inequality between ΔI_A and ΔI_D, which describes accumulation and dissipation, is reversed in these two regions. Thus, the beam intensity oscillations cannot be governed by the spatial distribution of the beam alone.

Figure 5c shows the reciprocal space profile of the same beam propagation with the same positions also marked by "R" and "F." The corresponding lateral profiles representing the angular distributions are shown in Figure 5d. In contrast to the spatial distributions, the angular distributions are significantly different within each pair. For points along the rise regions of the oscillations, the angular distribution is localized around $\alpha = 0$, which corresponds to the beam traveling increasingly parallel to the optic axis. Thus, in the rise regions where

$\Delta I_A > \Delta I_D$, the scattering centers are focusing the majority of the beam toward the atomic column. This rise behavior continues for as long as the condition $\Delta I_A > \Delta I_D$ is met. The inequality reverses when the intensity along the optic axis reaches a maximum. At this point, scattering centers begin to scatter the focused probe away from the atomic column because the average electron spatial distribution is below r_I (Fig. 4). This leads to an increase in electrons traveling away from the atomic column, and therefore, $\Delta I_A < \Delta I_D$, corresponding to the fall region. Angular distribution is now skewed toward larger α. Because the interaction of the beam electron with atoms of the column is based on an attractive Coulomb potential, electrons with large α traveling away from the atomic column will again be continuously focused by each scattering event. Subsequently, a majority of the electrons will again travel increasingly parallel to the atomic column (angular distribution is localized around $\alpha = 0$), allowing the cycle to begin anew. Thus, the cyclic behavior in the angular distribution leads to oscillations in spatial distribution or intensity along the optic axis. Therefore, the characteristics of intensity oscillations in channeling along high-Z columns, particularly the frequency of oscillations, must be significantly influenced by the severity of angular redistribution of the beam during scattering events.

Because the change in angular distribution occurs when atoms in the column scatter the propagating probe, it can be expected that the change in the angular distribution of the probe due to scattering is a function of the elemental composition of the atomic column. Figure 6a compares the
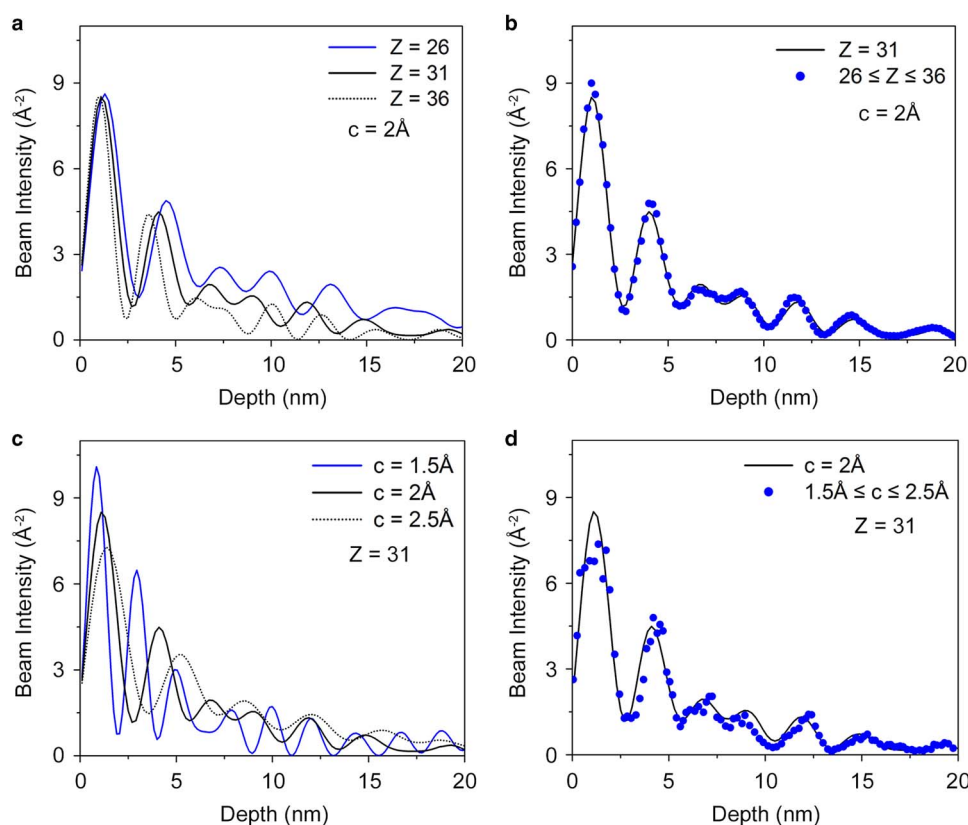
Figure 6. a: Beam intensity depth profiles of the same STEM probe in isolated columns with $Z = 26$, 31, and 36. **b:** Comparison of beam propagation along a column with Z randomly dispersed between 26 and 36 and that along an isolated column of Ga with $Z_{Ga} = 31$. The interatomic spacing is $c = 2$ Å in (**a**) and (**b**). **c:** Comparison of $Z_{Ga} = 31$ columns with $c = 1.5$ Å, 2 Å, and 2.5 Å interatomic spacing. **d:** Comparison of $Z_{Ga} = 31$ column with 2 Å spacing versus a column with random interatomic spacing between 1.5 Å and 2.5 Å (in these simulations, slice thickness of $\Delta z = 0.5$ A was used).

intensity profile of the beam propagating along isolated atomic columns of various Z with 0.2 nm interatomic spacing. In the first 20 nm, the beam undergoes 6, 7, and 8 intensity oscillations while propagating through atomic columns with $Z = 26$, 31, and 36, respectively (oscillations are determined by counting the number of peaks in the profile). Because higher Z increases the cross-section and the characteristic angle of scattering, high-Z atoms along the column will cause a greater angular redistribution of the propagating beam. The period of electrons scattering toward and away from the atomic column, as described above, will be shorter. Therefore, an electron probe propagating along a column with higher Z will experience higher frequencies of oscillations than those with lower Z. More interestingly, similar oscillatory behavior of the STEM probe is observed when the beam propagates through atomic columns containing multiple types of atoms but summing to the same average level of scattering, regardless of the Z value of each individual atom. Figure 6b compares the simulated STEM probe propagation along a column of Ga atoms ($Z_{Ga} = 31$) with that along a column of random elements between $Z = 26$ and $Z = 36$ while maintaining an average of $Z_{ave} = 31$. As can be seen, the oscillations are nearly identical. A probe propagating through a polyatomic column behaves as if the column contained an "averaged" element. Thus, the

beam channeling along the column is defined by the average, and not the exact, composition of the column.

Similar to atomic composition, interatomic spacing within a column also affects the intensity oscillations because it controls the amount of dissipation of the beam and the rate of scattering. Figure 6c compares intensity oscillations of a STEM probe propagating along a Ga column with 0.15, 0.2, and 0.25 nm spacing. In the first 20 nm, the probe experiences 9, 7, and 6 oscillations in the respective columns. Increasing the interatomic spacing reduces the number of atoms to scatter the propagating beam. As discussed previously, each scattering event changes the angular distribution of the beam, which focuses the STEM probe toward or away from the optic axis. Reducing the number of scattering events by increasing the atomic spacing in the column decreases the frequency of intensity oscillations, comparable with the consequences of decreasing the Z of scattering centers. Similar to the "averaged"-Z atomic column, a column with an "average" spacing of 0.2 nm shows nearly identical oscillations as an atomic column with periodic spacing of 0.2 nm, as shown in Figure 6d. Altogether, the comparisons between the "averaged" versus exact Z and interatomic spacing in Figures 6b and 6d show that beam intensity oscillations depend on a series of changes in the angular distribution, rather than on changes that are periodic with the host lattice. These results are consistent with the quantitative interpretation of high resolution transmission
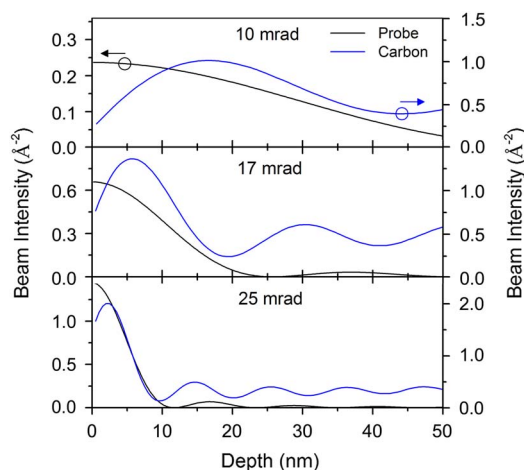
Figure 7. Beam intensity profile for STEM probes with various convergence angles propagating in isolated columns of C atoms with interatomic spacing of 5 Å.

electron microscopy (HRTEM) images and electron diffractions patterns by Van Dyck and Op de Beeck, showing the incident electron is only affected by an averaged atomic potential (Op de Beeck & Van Dyck, 1996; Van Dyck & Op de Beeck, 1996). Thus, beam channeling along the atomic column does not depend on the periodic nature of an atomic column or crystal, but rather on the accumulation of individual scattering events.

Intensity Oscillations in Low-Z Columns

As discussed previously, the beam does not strongly localize along an atomic column in low-Z crystals. However, beam propagation in a low-Z crystal can still be approximated by its behavior in an isolated atomic column because the weak scattering centers, whether in a crystal or an isolated column, only slightly alter the beam's behavior. The initial intensity of the STEM probe is quickly distributed to neighboring columns similar to the probe's behavior in vacuum (see Fig. 2). This suggests that the initial probe with its specific angular distribution defined by the convergence angle of the STEM probe governs the oscillations of the beam in the original column. Figure 7 shows beam intensity profiles of STEM probes with various convergence angles propagating along isolated columns of C atoms ($Z_C = 6$). The profiles are compared with those propagating in vacuum without a sample. Increasing a probe's convergence angle increases the frequency of intensity oscillations along the optic axis for propagation through vacuum or through an isolated C column. However, although these changes in the intensity oscillations are very similar, they are not identical. The atoms still slightly scatter the beam and cannot be entirely neglected when quantitative analysis is necessary. It should be noted that the energy of the electron probe also affects the initial angular redistribution of the beam (Lugg et al., 2011; Mittal, 2013). The frequency of oscillation can be expected to change for both propagations in an isolated C column and vacuum when the energy of the electron probe is varied, similar to changes in the convergence angle.
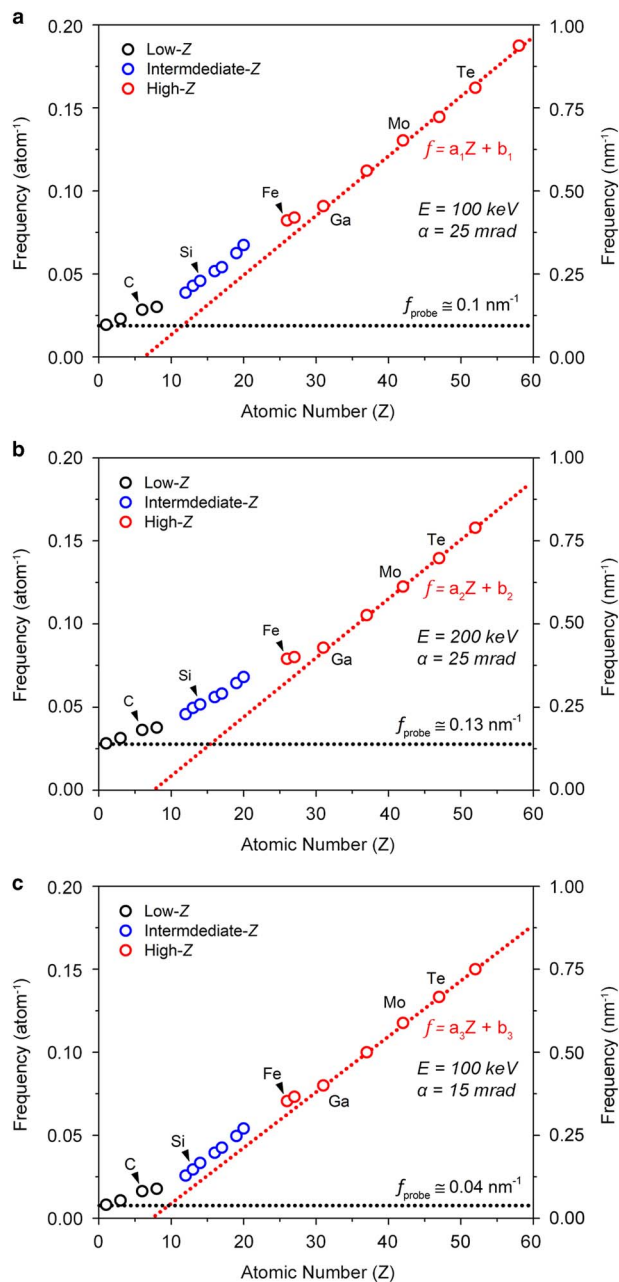

Figure 8. Frequency of oscillation in beam intensity along the optic axis in isolated atomic columns of different elements with interatomic spacing of 2 Å for three STEM probes: (**a**) $E_o = 100$ keV and $\alpha_{obj} = 25$ mrad, (**b**) $E_o = 200$ keV and $\alpha_{obj} = 25$ mrad, and (**c**) $E_o = 100$ keV and $\alpha_{obj} = 15$ mrad. The dotted black lines represent the frequency of oscillation of the probe in vacuum. The red dotted lines are linear fits of data points between $Z = 49$ to $Z = 70$ that are representative of very high-Z elements.

Generalizing Intensity Oscillations in Isolated Columns

Dependence on Atomic Number

The effects of Z on channeling of the beam along atomic columns can be compared for the entire range of atomic compositions by quantifying the oscillations of the incident STEM probe. Figure 8a summarizes the frequency of

oscillations across a broad range of Z values, for which the frequencies were determined by counting the number of peaks in the beam intensity profiles. Three distinct regimes can be observed. In the high-Z regime ($Z \gtrsim 26$), where the atomic scattering dominates angular redistribution, a linear dependence between the frequency of oscillations and Z can be observed, similar to those predicted earlier (Van Dyck & Op de Beeck, 1996). In contrast, in the low-Z regime ($Z \lesssim 9$), the scattering centers are weak and the beam behaves nearly as it would in vacuum without a specimen. The frequency of oscillation in an isolated column, f_{ic}, in this regime can be treated as nearly constant and is only a function of the initial probe parameters, $f_{ic} \approx f_p$, where $f_p (E_o, \alpha_{obj})$ is the frequency of oscillation of a probe at a given energy, E_o, and convergence angle, α_{obj}. Between the two regimes of high-Z and low-Z atoms, there is a regime of intermediate-Z ($10 \lesssim Z \lesssim 25$) in which the frequency of oscillation cannot be well approximated as a constant (low Z) or as a linear dependence (high Z). Here, the frequency of oscillations becomes sensitive to details of the electronic configuration of the atomic potential, which greatly affect the cross-sections of elastic scattering (Kirkland, 2010; Egerton, 2011). These intermediate-Z atoms have a considerable effect on the frequency of oscillation but are not strong enough to focus the majority of the electron beam like those in the high-Z regime (Fig. 2). Thus, electron propagation in an intermediate-Z column shows mixed behavior.

Dependence on Probe Parameters

To accommodate a wider range of experimental conditions, simulations were performed to study how the frequency of oscillations changes with probe conditions. Figures 8b and 8c show the frequencies as a function of Z with a change in energy and convergence angle. Raising the energy of the electron beam, as shown in Figure 8b, increases f_p from 0.10 to 0.13 nm. Similarly, lowering the convergence angle, as shown in Figure 8c, decreases f_p from 0.10 to 0.04 nm. In both cases, the exact values of the frequencies change across the entire Z range, but the constant and linear behavior at low and high Z, respectively, are still apparent. Thus, regardless of the initial parameters of the beam, Z-dependence of the frequency of oscillation can still be separated into the three distinct regimes discussed previously.

The similarity between the results in Figures 8a to 8c suggests that changing the probe parameters merely shifts the entire range of frequencies by f_p. To study the effects of probe parameters further, the f_p-subtracted frequency are summarized in Figure 9a. The low- and intermediate-Z regime frequencies are nearly identical for all simulated probe parameters. The high-Z regime frequencies show slightly increasing deviations with increasing Z, but a linear fit of the high-Z frequencies (Fig. 9b) simulated at each probe parameter reveals that the differences in slope and intercept are small despite the wide range of convergence angles and accelerating voltages considered.
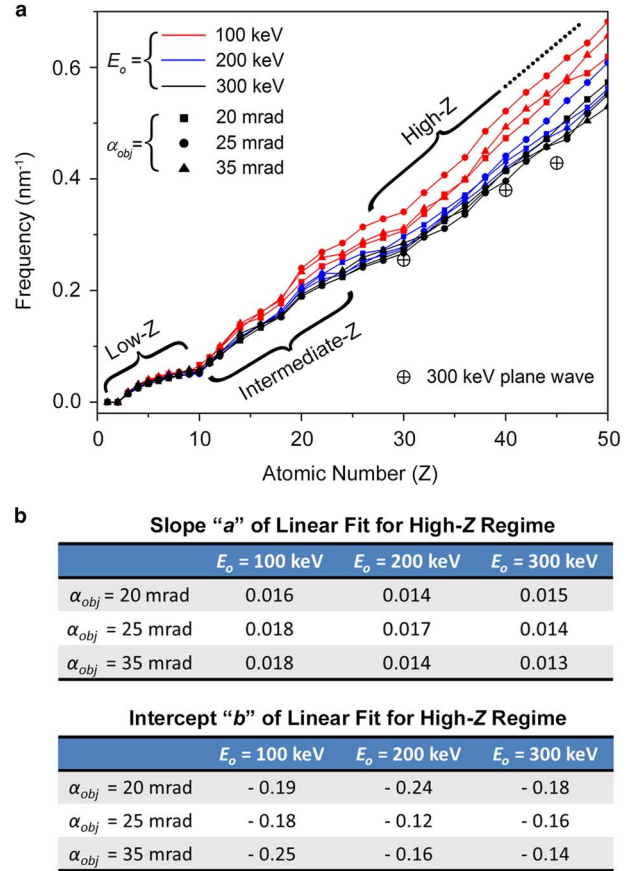

Figure 9. a: Frequency of oscillation in beam intensity along the optic axis in isolated atomic columns of different elements with interatomic spacing of 2 Å subtracted by the frequency of beam propagating in vacuum. Frequency of plane wave oscillations at 300 keV are included for comparison. **b:** The slopes and intercepts of the linear fits in the high-Z regime.

Slope "a" of Linear Fit for High-Z Regime

	E_o = 100 keV	E_o = 200 keV	E_o = 300 keV
α_{obj} = 20 mrad	0.016	0.014	0.015
α_{obj} = 25 mrad	0.018	0.017	0.014
α_{obj} = 35 mrad	0.018	0.014	0.013

Intercept "b" of Linear Fit for High-Z Regime

	E_o = 100 keV	E_o = 200 keV	E_o = 300 keV
α_{obj} = 20 mrad	- 0.19	- 0.24	- 0.18
α_{obj} = 25 mrad	- 0.18	- 0.12	- 0.16
α_{obj} = 35 mrad	- 0.25	- 0.16	- 0.14

This uniformity of the results suggests the frequency of oscillation for the entire range of Z for isolated columns can be approximated as:

$$f_{ic}(Z, E_o, \alpha_{obj}) = f_p(E_o, \alpha_{obj}) + f_{sc}(Z, E_o, \alpha_{obj}), \qquad (1)$$

where $f_{sc}(Z, E_o, \alpha_{obj})$ is the contribution from the single column. This approximation is further tested by comparing $f_{sc}(Z, E_o, \alpha_{obj})$ at a few Z values to the frequencies of oscillations for plane waves propagating along the same atomic column (see Fig. 9a), where $f_p(E_o, \alpha_{obj}) \sim 0$ for plane waves. In the low-Z regime, where $f_p \gg f_{sc}$, equation (1) simplifies to:

$$f_{ic}(Z, E_o, \alpha_{obj}) = f_p(E_o, \alpha_{obj}). \qquad (2)$$

In the high-Z regime, $f_{sc}(Z, E_o, \alpha_{obj})$ is approximately linear in Z, and equation (1) can be expressed as:

$$f_{ic}(Z, E_o, \alpha_{obj}) = f_p(E_o, \alpha_{obj}) + a \times Z + b, \qquad (3)$$

where a and b are weak functions of E_o and α_{obj}. In the intermediate-Z regime, no simple approximations can be made beyond that $f_{sc}(Z, E_o, \alpha_{obj})$ is a weak function of E_o and α_{obj}.
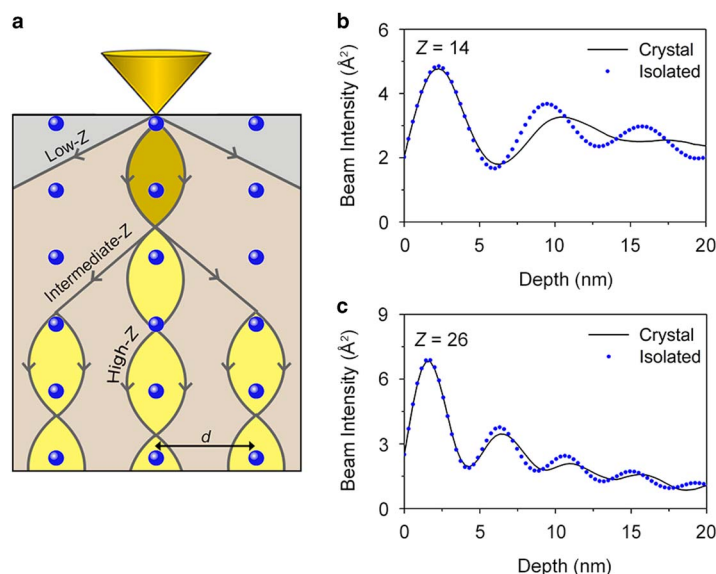
Figure 10. a: Simple schematic diagram showing the paths of the beam intensity from the STEM probe as it propagates in low-, intermediate- and high-Z crystals. **b:** Comparison of beam intensity depth profiles for a STEM probe propagating along a hypothetical [001]-oriented BCC Si crystal and in an isolated column of Si, which represents an intermediate-Z case. **c:** Comparison of beam intensity depth profiles for a STEM probe propagating along a [001]-oriented BCC Fe crystal and in an isolated column of Fe, which represents a high-Z case.

Generalizing Intensity Oscillations for Crystals

Dependence on Atomic Number and Probe Parameters
Beam propagation in isolated columns approximates that in actual crystals. Thus, it is important to show how equation (1) is applicable to a crystal. Equation (1) and the three distinct Z regimes can be better understood by tracking the path of the beam during propagation in a crystal. Figure 10a shows a schematic of the beam path during propagation in crystals of different Z. During propagation in a low-Z crystal, the majority of the beam continuously spreads throughout the crystal because the scattering centers cannot trap or focus the beam. Therefore, a probe propagating in a low-Z crystal continuously distributes its intensity to neighboring columns. The frequency of the beam oscillation in a crystal, f_{cry}, during channeling both along the optic axis and in neighboring columns can be approximated as that in vacuum, f_p. Therefore, equation (1) for a crystal can also be simplified to $f_{ic}(Z, E_o, \alpha_{obj}) = f_p(E_o, \alpha_{obj})$ analogous to equation (2) corresponding to an isolated column. In a high-Z crystal, on the other hand, the electron beam is localized on the original column because the strong scattering centers focus the beam. The atoms of the column that is along the optic axis affect the propagating STEM probe and govern the frequency of oscillations during channeling. Therefore, $f_{cry}(Z, E_o, \alpha_{obj}) = f_{ic}(Z, E_o, \alpha_{obj}) = f_p(E_o, \alpha_{obj}) + a \times Z + b$.

The behavior of the propagating beam in intermediate-Z crystals is a combination of the low- and high-Z regimes. Here, the beam partially channels along the original column as it would in a high-Z crystal and partially spreads, as it would in a low-Z crystal. The neighboring columns also have a sufficient attractive Coulombic potential to trap or focus part of the beam before the beams spreads again. The beam

spreading and focusing are two competing mechanisms during propagation in a crystal in intermediate-Z crystals. Thus, in the intermediate-Z case, $f_{cry} \neq f_{ic}$. This can be seen in the intensity line scan in Figure 10b for Si ($Z = 14$) where the amplitude and frequency of oscillation of the beam in the crystal and isolated column do not match. Furthermore, $f_{cry}(Z, E_o, \alpha_{obj})$ may not be a weak function of E_o and α_{obj} as the distance between columns start to play a bigger role.

It may be helpful to determine where the intermediate- and high-Z regimes overlap. Figure 10c shows the line scan comparison for Fe ($Z = 26$) which shows a relatively small difference between the crystal and the isolated column. This discrepancy is smaller than that for Si in Figure 10b as expected with increased Z. Because the depth profile of the probe propagating in an α-Fe crystal (Fig. 2) shows that the beam is localized on the original atomic column, it can be proposed that $Z = 26$ is approximately the boundary separating intermediate- and high-Z for the wide range of STEM probe energy (100–300 keV) and convergence angles (15–35 mrad). However, this boundary may be slightly different for other STEM probes.

Dependence on Intercolumn Spacing
As discussed previously, in crystals with intermediate-Z, the distance between individual columns, d, (Fig. 10a) also affects the channeling behavior of the beam. Figure 11 shows simulated depth profiles of electron probes propagating within α-Fe crystals with various intercolumn spacing. At $d = 0.2$ nm, which corresponds to the intercolumn spacing in natural α-Fe (lattice parameter = 0.286 nm) (Davey, 1925), the probe intensity is localized to the original column as expected because Fe is in the high-Z regime. However, as the intercolumn spacing decreases, the Coulomb potential
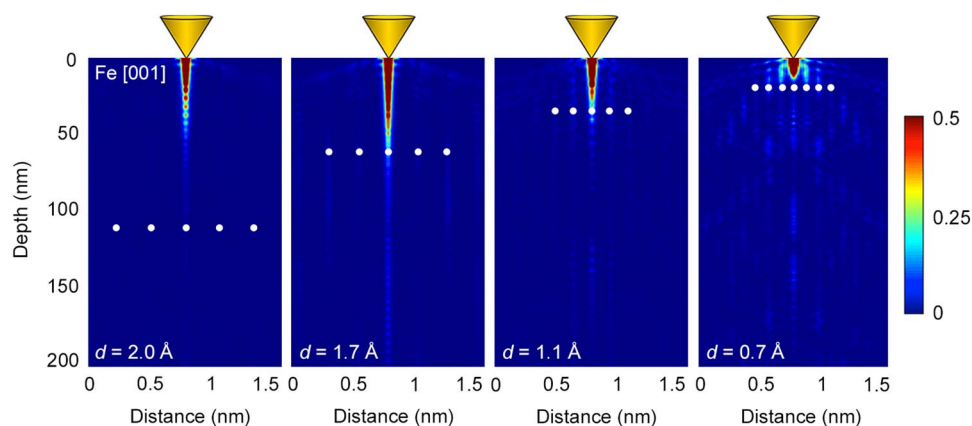
Figure 11. 2D beam intensity depth profiles of simulated STEM probes propagating in α-Fe crystals with various inter-column spacing, d, along the [001] crystallographic zone axis. The cross sections are along the [100] direction (x-axis) perpendicular to the incident beam direction (z-axis). The solid circles mark positions of atomic columns. $d = 2.0$ Å corresponds to the inter-column spacing in α-Fe with the natural lattice parameter $= 2.86$ Å (Davey, 1925).

from other columns starts to attract and trap portions of the beam, and the depth profile of a beam propagating in such a crystal begins to resemble that in an intermediate-Z case. At $d \lesssim 0.07$ nm, rather than channeling only along the original column, the propagating beam spreads to neighboring columns continuously, similar to intermediate-Z or even low-Z cases. Thus, the boundaries of the low-, intermediate-, and high-Z regimes are dependent on the intercolumn spacing, particularly when the intercolumn spacing becomes very small. These observations suggest that when imaging most of the known crystals along the main (low-order) crystallographic orientations, the effects of neighboring columns can be ignored because the intercolumn distances are relatively large (~0.2 nm). However, when these high-Z crystals are viewed along high-order zone axis with small intercolumn spacing, the neighboring effects should be taken into account.

Intensity Reversal due to Oscillations

An understanding of STEM probe channeling in isolated atomic columns can be used to predict counterintuitive results in high-resolution ADF-STEM images or in STEM-EDX (energy dispersive x-ray spectroscopy) maps of real materials. For example, in extensively studied GaAs, when the crystal is imaged along the [110] direction using ADF-STEM, columns of As ($Z_{As} = 33$) should appear more intense than columns of Ga ($Z_{Ga} = 31$) according to the conventional Z-contrast theory of ADF-STEM imaging (Pennycook & Jesson, 1991). Figure 12a shows simulated 2D depth profiles of a STEM beam (without considering thermal displacements) propagating along a Ga column and a neighboring As column in the [110] direction of a GaAs crystal. Both profiles show that the beam is confined to the original column, which is consistent with the previous discussion of beam behavior in high-Z atomic columns. Figure 12b compares the beam intensity along the optic axis during the propagation along both columns. Because Z_{Ga} and Z_{As} are slightly different, the higher Z of As leads to a

slighter higher frequency of oscillation. This small difference is sufficient to change the location of the rise and fall regions of the beam, which becomes more noticeable at larger depths (>20 nm). At ~25 nm, the rise region for the beam propagating in As corresponds to a fall region in Ga. Thus, at certain thicknesses, the incident electron beam intensity is higher in the Ga column than in As. As the beam propagates further down the column, these intensity offsets cause differences in total beam interactions between Ga and As columns, which ultimately cause a nonintuitive intensity reversal in the ADF-STEM signal (Fig. 12c). For specimens thinner than ~35 nm, the As column appears more intense than Ga, but for thicknesses greater than ~ 45 nm, the Ga column actually appears more intense despite possessing a lower Z.

This intensity reversal is present even at low finite temperatures, as shown in Figures 12d to 12f for 100 K, in which thermal displacements of atoms are taken into account using the frozen-phonon approximation (Loane et al., 1991). At finite temperatures, the beam intensity oscillations are dampened, as is expected, and the intensity reversal becomes less apparent compared with the thermal-diffuse scattering-free results. These differences suggest that at higher temperatures, the intensity reversal may disappear entirely because the thermal displacements of atoms increase with temperature. Figure 13 compares the intensity ratios between a column of Ga and As as a function of depth for various temperatures, where a ratio above 1 indicates intensity reversal. At 63 K (melting point of nitrogen) and 100 K, intensity reversal exists at thicknesses greater than ~70 nm. Above this thickness, ADF-STEM images of GaAs taken along the [110] direction will show Ga columns with greater intensity than the As columns. For 200 and 300 K, the intensity ratio is <1 over the entire simulated thickness range (1–80 nm). Thus, ADF-STEM images of GaAs collected at room temperature (~300 K) provide chemical information according to conventional Z-contrast behavior. However, based on the temperature dependence of this intensity reversal phenomenon, it can be proposed that there may be
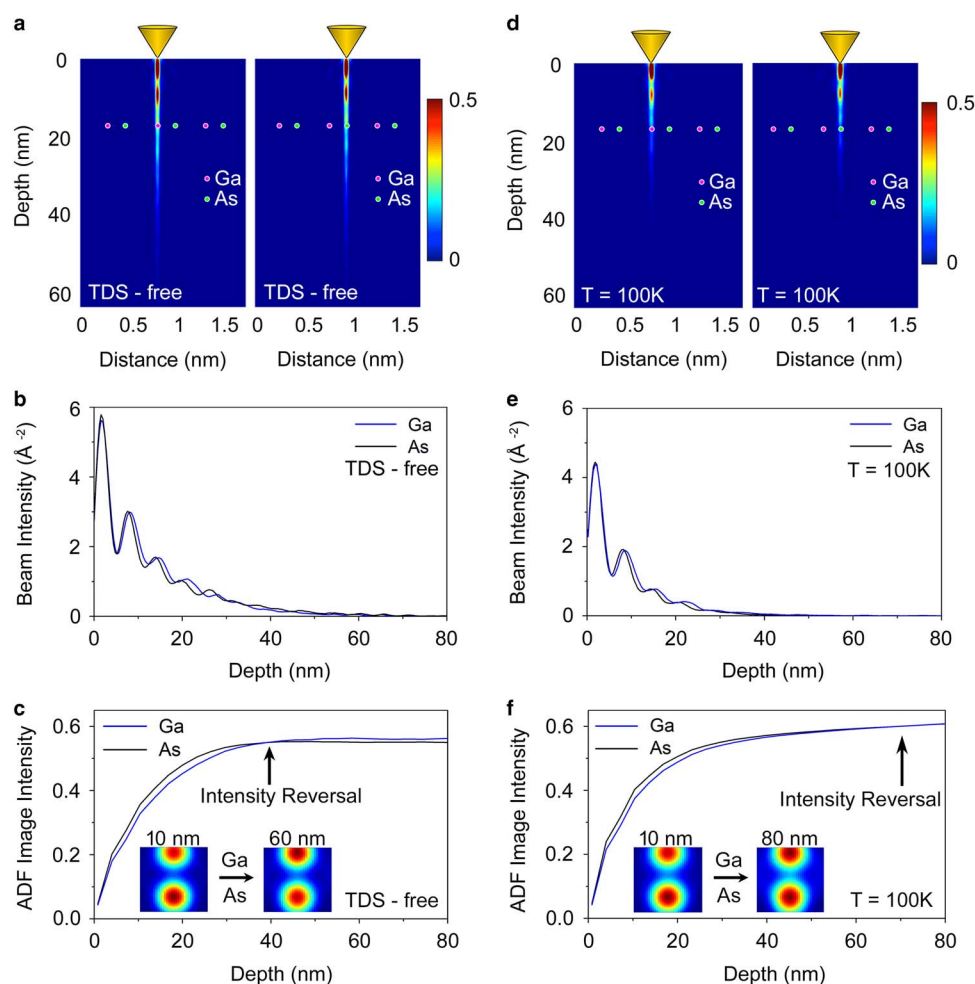
Figure 12. a: 2D beam intensity depth profiles of a simulated STEM probe propagating in the [110] direction of a GaAs crystal without thermal diffuse scattering (TDS-free), using two separate probes positioned on a Ga column and an As column. **b:** Corresponding beam intensity depth profiles along the optic axis. **c:** ADF intensity depth profile with intensities normalized to the incident beam. Inner and outer ADF detector angles used in these simulations were 50 and 200 mrad, respectively. Insets show ADF-STEM images of a pair of Ga and As atomic columns for 10 and 60 nm thick samples where the intensity reversal is visible. **d–f:** Corresponding to (a–c) results at T = 100 K with implementation of 100 frozen phonon configurations. These simulations were performed on $32 \times 32 \, \text{Å}^2$ supercells using $1024 \times 1024 \, \text{pixel}^2$ grids for transmission and probe functions. In T = 100 K simulations, root-mean-square thermal displacements (RMSD) of 0.058 Å (Schowalter et al., 2009) and 0.054 Å (Schowalter et al., 2009) for each site of Ga and As, respectively, were used.

materials, especially those with lower Debye–Waller factors, for which this intensity reversal can occur even at room temperature. In those cases, chemical identification based solely on Z-contrast would lead to an incorrect result, and parallel recording of STEM-EDX or STEM-EELS (electron energy loss spectroscopy) maps would then be necessary to identify the columns. These results are consistent with those observed by (LeBeau et al., 2009) on $PbWO_4$ where atomic number alone was insufficient for interpreting image contrast. The strong focusing of the STEM probe along these high-Z columns should still localize the generated EDX or EELS signals to the original column. Thus, STEM-EDX and STEM-EELS maps produced this way will produce reliable identification of the columns, whereas ADF-STEM imaging alone will not.

CONCLUSION

Simulated beam intensity profiles of STEM probes propagating through low-Z, intermediate-Z, and high-Z crystals show considerable differences in their beam channeling behavior. These differences demonstrate that the atomic number of the crystal is a key parameter that governs beam intensity oscillations and allows the separation of crystals into distinct regimes. In high-Z crystals ($Z \gtrsim 26$), when the STEM probe is placed on an atomic column, beam intensity oscillations occur only along that column. In this regime, the angular redistribution of the beam due to atomic scattering significantly affects the frequency of beam oscillations. Increasing Z or decreasing the interatomic spacing within the isolated column both lead to higher frequencies of
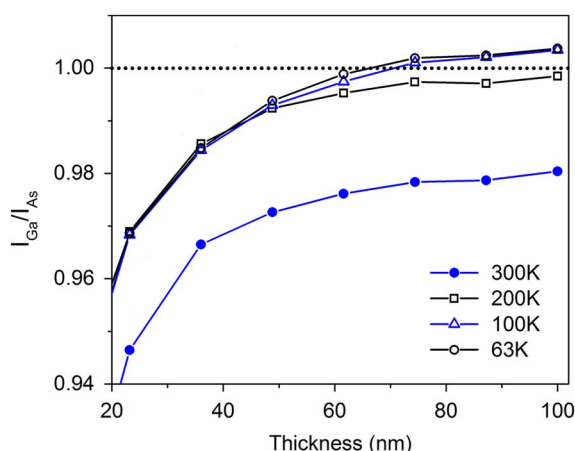
Figure 13. Ratio of ADF intensities from Ga and As atomic columns simulated at temperatures of 63 K, 100 K, 200 K and 300 K. Intensity ratio greater than 1 (dotted line) indicates an intensity reversal between the Ga and As columns. ADF intensity that is averaged across the central 4×4 pixels^2 of the simulated atomic columns is used here. Temperature-dependent RMSD values were used in these simulations (Schowalter et al., 2009). All other simulation parameters follow those reported in Figure 12.

Multislice simulations were performed using computational resources provided by the Minnesota Supercomputing Institute at the University of Minnesota.

intensity oscillations. In addition, beam intensity oscillations appear to be a result of a series of changes in the angular distribution of the beam rather than an effect due to the periodic nature of the crystal. In low-Z crystals ($Z \lesssim 9$), the beam spreads throughout the crystal, and its intensity oscillates along atomic columns at a frequency largely governed by the probe and its initial angular distribution. For intermediate Z ($10 \lesssim Z \lesssim 25$), however, proper accounting of the initial conditions of the beam, as well as the elemental composition of the crystal, is necessary in order to properly predict beam channeling. The frequency of oscillation during beam propagation in crystals of all Z can be approximated as a summation of the contributions from the probe and scattering from atoms. Furthermore, this description appears to hold for a wide range of probe energies and convergence angles. For crystals with either high-Z or low-Z atoms, an understanding of beam channeling through a simpler model, using isolated atomic columns, can be used to explain or predict unusual, and in some cases nonintuitive, phenomena. In these cases, it can be proposed that inferring chemical information solely from an ADF-STEM image without a proper understanding of intensity oscillations arising from channeling may lead to erroneous conclusions.

Acknowledgment

References

Borisevich, A.Y., Lupini, A.R. & Pennycook, S.J. (2006). Depth sectioning with the aberration-corrected scanning transmission electron microscope. *Proc Natl Acad Sci U S A* **103**, 3044–3048.

Cowley, J.M. & Moodie, A.F. (1957). The scattering of electrons by atoms and crystals: A new theoretical approach. *Acta Crystallogr A* **10**, 609–619.

D'Alfonso, A.J., Findlay, S.D., Oxley, M.P., Pennycook, S.J., van Benthem, K. & Allen, L.J. (2007). Depth sectioning in scanning transmission electron microscopy based on core-loss spectroscopy. *Ultramicroscopy* **108**, 17–28.

Davey, W.P. (1925). Precision measurements of the lattice constants of twelve common metals. *Phys Rev Lett* **25**, 753–761.

Egerton, R.F. (2011). *Electron Energy Loss Spectroscopy in the Electron Microscope*, 3rd ed. New York: Springer.

Ewald, P. P. (1921). Die Berechnung optischer und elektrostatischer Gitterpotentiale. *Ann Phys* **369**, 253–287.

Fertig, J. & Rose, H. (1981). Resolution and contrast of crystalline objects in high-resolution scanning transmission electron microscopy. *Optik* **59**, 407–429.

Giannozzi, P., Baroni, S., Bonini, N., Calandra, M., Car, R., Cavazzoni, C., Ceresoli, D., Chiarotti, G.L., Cococcioni, M., Dabo, I., Corso, A.D., de Gironcoli, S., Fabris, S., Fratesi, G., Gebauer, R., Gerstmann, U., Gougoussis, C., Kokalj, A., Lazzeri, M., Martin-Samos, L., Marzari, N., Mauri, F., Mazzarello, R., Paolini, S., Pasquarello, A., Paulatto, L., Sbraccia, C., Scandolo, S., Sclauzero, G., Smogunov, A.P., Umari, P. & Wentzcovitch, R.M. (2009). QUANTUM ESPRESSO: a modular and open-source software project for quantum simulations of materials. *J Phys Condens Matter* **21**, 399502.

Haruta, M., Kurata, H., Komatsu, H., Shimakawa, Y. & Isoda, S. (2009). Effects of electron channeling in HAADF-STEM intensity in La$_2$CuSnO$_6$. *Ultramicroscopy* **109**, 361–367.

Hillyard, S., Loane, R.F. & Silcox, J. (1993). Annular dark-field imaging: Resolution and thickness effects. *Ultramicroscopy* **49**, 14–25.

Hillyard, S. & Silcox, J. (1993). Thickness effects in ADF STEM zone axis images. *Ultramicroscopy* **52**, 325–334.

Hillyard, S. & Silcox, J. (1995). Detector geometry, thermal diffuse scattering and strain effects in ADF STEM imaging. *Ultramicroscopy* **58**, 6–17.

Hovden, R., Xin, H.L. & Muller, D.A. (2012). Channeling of a subangstrom electron beam in a crystal mapped to two-dimensional molecular orbitals. *Phys Rev B* **86**, 195415.

Hwang, J., Zhang, J.Y., D'Alfonso, A.J., Allen, L.J. & Stemmer, S. (2013). Three-dimensional imaging of individual dopant atoms in SrTiO$_3$. *Phys Rev Lett* **111**, 266101.

Ishikawa, R., Lupini, A.R., Findlay, S.D., Taniguchi, T. & Pennycook, S.J. (2014). Three-dimensional location of a single dopant with atomic precision by aberration corrected scanning transmission electron microscopy. *Nano Lett* **14**, 1903–1908.

Kambe, K., Lehmpfuhl, G. & Fujimoto, F. (1974). Interpretation of electron channeling by the dynamical theory of electron diffraction. *Z Naturforschung* **29**, 1034–1044.

Kirkland, E.J. (2010). *Advanced Computing in Electron Microscopy*, 2nd ed New York: Springer.

Komaki, K. & Fujimoto, F. (1974). Quantized rosette motion of energetic electron around an atomic row in crystal. *Phys Lett A* **49**, 445–446.

Kourkoutis, L.F., Parker, M.K., Vaithyanathan, V., Schlom, D.G. & Muller, D.A. (2011). Direct measurement of electron channeling in a crystal using scanning transmission electron microscopy. *Phys Rev B* **84**, 075485.

Kreiner, H.J., Bell, F., Sizmann, R., Harder, D. & Hüttl, W. (1970). Rosette motion in negative particle channeling. *Phys Lett A* **33**, 135–136.

LeBeau, J.M., Findlay, S.D., Allen, L.J. & Stemmer, S. (2008). Quantitative atomic resolution scanning transmission electron microscopy. *Phys Rev Lett* **100**, 206101.

LeBeau, J.M., Findlay, S.D., Wang, X., Jacobson, A.J., Allen, L.J. & Stemmer, S. (2009). High-angle scattering of fast electrons from crystals containing heavy elements. *Phys Rev B* **79**, 214110.

LeBeau, J.M., Findlay, S.D., Allen, L.J. & Stemmer, S. (2010). Standardless atom counting in scanning transmission electron microscopy. *Nano Lett* **10**, 4405–4408.

Lindhard, J. (1965). Influence of crystal lattice on the motion of energetic charged particles. *Kongel Dan Vidensk Selsk Mat Fys Medd* **34**, 14.

Loane, R.F., Kirkland, E.J. & Silcox, J. (1988). Visibility of single heavy atoms on thin crystalline silicon in simulated annular dark-field STEM images. *Acta Crystallogr Sect A* **44**, 912–927.

Loane, R.F., Xu, P. & Silcox, J. (1991). Thermal vibrations in convergent-beam electron diffraction. *Acta Crystallogr A* **47**, 267–278.

Lugg, N.R., Findlay, S.D., Shibata, N., Mizoguchi, T., D'Alfonso, A.J., Allen, L.J. & Ikuhara, Y. (2011). Scanning transmission electron microscopy imaging dynamics at low accelerating voltages. *Ultramicroscopy* **111**, 999–1013.

Mittal, A. (2013). A theoretical study of dopant atom detection and probe behavior in STEM. PhD Thesis. University of Minnesota, Minneapolis, MN.

Mittal, A. & Mkhoyan, K.A. (2011). Limits in detecting an individual dopant atom embedded in a crystal. *Ultramicroscopy* **111**, 1101–1110.

Mkhoyan, K.A., Maccagnano-Zacher, S.E., Kirkland, E.J. & Silcox, J. (2008). Effects of amorphous layers on ADF-STEM imaging. *Ultramicroscopy* **108**, 791–803.

Nellist, P.D. & Pennycook, S.J. (1999). Incoherent imaging using dynamically scattered coherent electrons. *Ultramicroscopy* **78**, 111–124.

Odlyzko, M.L., Held, J.T. & Mkhoyan, K.A. (2016). Atomic bonding effects in annular dark field scanning transmission electron microscopy. II. Experiments. *J Vac Sci Technol A* **34**, 041603.

Op de Beeck, M. & Van Dyck, D. (1996). Direct structure reconstruction in HRTEM. *Ultramicroscopy* **64**, 153–165.

Pennycook, S.J. (1988). Delocalization corrections for electron channeling analysis. *Ultramicroscopy* **26**, 239–248.

Pennycook, S.J. & Jesson, D.E. (1991). High-resolution Z-contrast imaging of crystals. *Ultramicroscopy* **37**, 14–38.

Perdew, J.P., Burke, K. & Ernzerhof, M. (1996). Generalized gradient approximation made simple. *Phys Rev Lett* **77**, 3865–3868.

Schowalter, M., Rosenauer, A., Titantah, J.T. & Lamoen, D. (2009). Computation and parametrization of the temperature dependence of Debye-Waller factors for group IV, III-V, and II-VI semiconductors. *Acta Crystallogr A* **65**, 5–17.

Sinkler, W. & Marks, L.D. (1999). A simple channelling model for HREM contrast transfer under dynamical conditions. *J Microsc* **194**, 112–123.

Tsyganov, E.N. (1976). Some aspects of the mechanism of a charge particle penetration through a monocrystal. In *Fermilab*. Batvia, IL: Fermi National Accelator Laboratory.

van den Bos, K.H.W., De Backer, A., Martinez, G.T., Winckelmans, N., Bals, S., Nellist, P.D. & Van Aert, S. (2016). Unscrambling mixed elements using high angle annular dark field scanning transmission electron microscopy. *Phys Rev Lett* **116**, 246101.

Van Aert, S., Geuens, P., Van Dyck, D., Kisielowski, C. & Jinschek, J.R. (2007). Electron channeling based crystallography. *Ultramicroscopy* **107**, 551–558.

Van Dyck, D. & Op de Beeck, M. (1996). A simple intuitive theory for electron diffraction. *Ultramicroscopy* **64**, 99–107.

Voyles, P.M., Grazul, J.L. & Muller, D.A. (2003). Imaging individual atoms inside crystals with ADF-STEM. *Ultramicroscopy* **96**, 251–273.

Voyles, P.M., Muller, D.A. & Kirkland, E.J. (2004). Depth-dependent imaging of individual dopant atoms in silicon. *Microsc Microanal* **10**, 291–300.

Wu, R.J., Odlyzko, M.L. & Mkhoyan, K.A. (2014). Determining the thickness of atomically thin MoS_2 and WS_2 in the TEM. *Ultramicroscopy* **147**, 8–20.

Xu, P., Loane, R.F. & Silcox, J. (1991). Energy-filtered convergent-beam electron diffraction in STEM. *Ultramicroscopy* **38**, 127–133.

Yu, Z. & Silcox, J. (2004). Channeling of sub-angstrom probes along isolated atomic columns. *Microsc Microanal* **10**(S02), 570–571.

Appendix A: Channeling of Aberration-Free and Aberration-Corrected Probes

For simplicity in this report, "ideal" or aberration-free STEM probes with identical electron energy and objective aperture were used in many simulations, instead of aberration-corrected probes. To evaluate the applicability of this simplification, two probes were generated, and their propagation through isolated atomic columns was simulated. For the "ideal" or aberration-free STEM probes, the following parameters were used: beam energy of $E_o = 100$ keV, $\alpha_{obj} = 25$ mrad, $Cs_{(3)} = 0$, $Cs_{(5)} = 0$, and defocus of $\Delta f = 0$. For the aberration-corrected probe, the following parameters were used: $E_o = 100$ keV, $\alpha_{obj} = 25$ mrad, $Cs_{(3)} = -0.015$ mm, $Cs_{(5)} = 10$ mm, and $\Delta f = -3$ nm. The results of simulations are presented in Figure A.1. Here both probes were propagated through an isolated column of Ge atoms with 0.2 nm interatomic spacing and a column of C atoms with 0.5 nm interatomic spacing. As can be seen, the shapes of the two probes and their channeling behavior are practically indistinguishable.
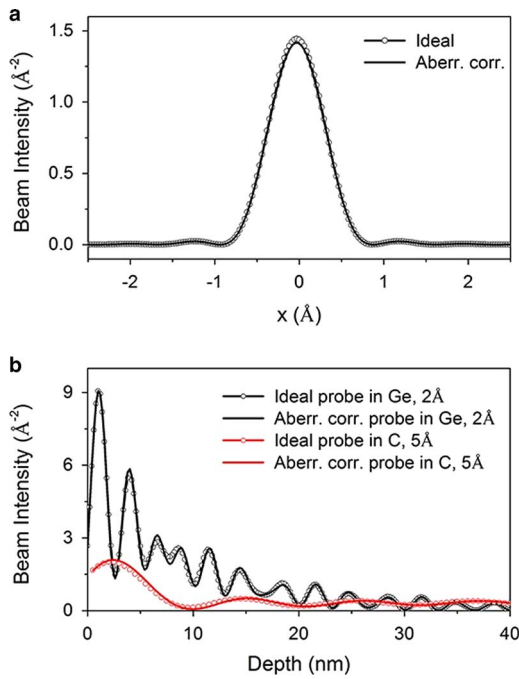
Figure A.1. a: Simulated shapes of "ideal" or aberration-free and aberration-corrected STEM probes with identical electron energy and objective aperture: $E_0 = 100$ keV and $a_{obj} = 25$ mrad. **b**: Beam intensity profiles of two probes propagation through an isolated column of Ge atoms with interatomic spacing 2 Å and a column of C atoms with interatomic spacing of 5 Å.
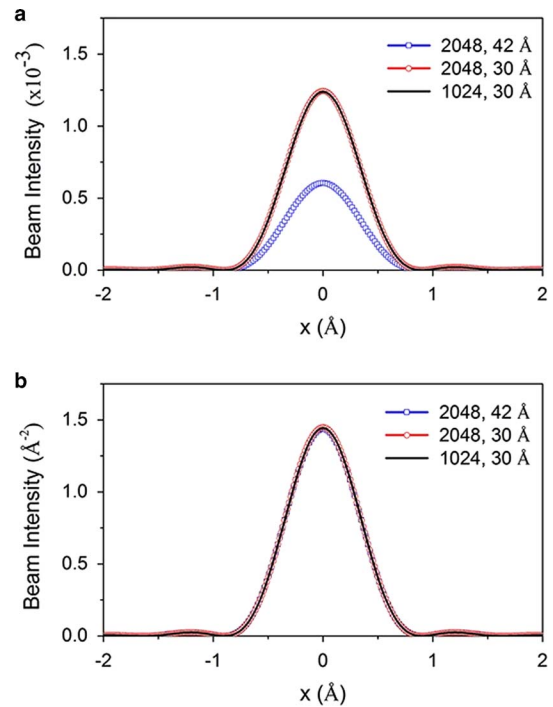

Figure A.2. Line scans of simulated $E_0 = 100$ keV and $a_{obj} = 25$ mrad aberration-free STEM probe using 1024×1024 pixels^2 in a 30×30 Å^2 supercell, 2048×2048 pixels^2 in a 42×42 Å^2 supercell, and 2048×2048 pixels^2 in a 30×30 Å^2 supercell that are normalized (**a**) using the old standard approach, Eq. (A1), and (**b**) using the normalization approach introduced above, Eq. (A3).

APPENDIX B: NORMALIZATION OF BEAM INTENSITY

One approach to normalize the beam intensity simulated using *multislice* programs developed by Kirkland (2010), which is a commonly accepted approach and the default setting of the TEMSIM code, is

$$I_{i,j}^{norm} = \frac{I_{i,j}}{\sum_{i=1}^{N_x} \sum_{j=1}^{N_y} I_{i,j}} = \frac{I_{i,j}}{N_x \times N_y}, \qquad (A.1)$$

where N_x and N_y are number of pixels in the x and y direction, respectively, and $I_{i,j}$ the intensity of pixel (i,j). The purpose of the normalization is to let the total integrated intensity of the incident probe be equal to 1:

$$\sum_{i=1}^{N_x} \sum_{j=1}^{N_y} I_{i,j}^{norm} = 1. \qquad (A.2)$$

The challenge is that this approach makes the values of normalized intensities sensitive to the pixel size used in the simulation. For comparison of the results from different simulations, one has to keep the same simulation grid across the samples. To avoid this constraint, we introduce an alternative normalization approach. Now, the intensity of pixel (i,j) is normalized according to the following:

$$I_{i,j}^{norm, new} = \frac{I_{i,j}}{a \times b}, \qquad (A.3)$$

where a and b are the supercell dimensions in the x and y directions, respectively. Although this approach creates normalized intensities in nm^{-2} or Å^{-2} units, it is independent of simulation sampling details and, therefore, is more robust and provides compatibility of results from different simulations. The total integrated intensity of the incident probe continues to be 1.

$$\sum_{i=1}^{N_x} \sum_{j=1}^{N_y} I_{i,j}^{norm, new} \times \Delta x_i \times \Delta y_j = 1, \qquad (A.4)$$

where $\Delta x_i \times \Delta y_j$ is the area of pixel (i,j)

To compare these two approaches of beam intensity normalization, we simulated $E_o = 100$ keV and $\alpha_{obj} = 25$ mrad aberration-free STEM probes using the following: (i) $1,024 \times 1,024$ pixels^2 in a 3.0×3.0 nm^2 supercell, (ii) $2,048 \times 2,048$ pixels^2 in a 4.2×4.2 nm^2 supercell, and (iii) $2,048 \times 2,048$ pixels^2 in 3.0×3.0 nm^2 supercell. Line scans of the probes plotted in Figure A.2 show that the more commonly accepted normalization method, equation (A.1), is independent of real space pixel size and is sensitive to reciprocal space pixel size (Fig. A.2a), whereas the new approach, equation (A.3), rescales the intensities independently of simulation grid size (Fig. A.2b).
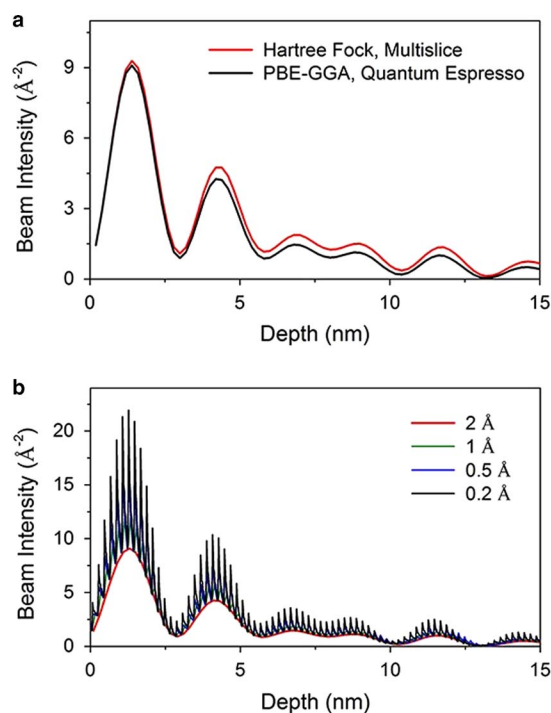
Figure A.3. Beam intensity profiles of an $E_0 = 100$ keV and $a_{obj} = 25$ mrad aberration-free STEM probe in an isolated column of Ge with interatomic spacing 2 Å and slice thickness 2 Å. **a**: Comparison of two methods used to calculate projected atomic potentials: (i) integration along the entire z-axes with 3D atomic potentials calculated using the Hartree–Fock approximation (standard *multislice* approach (Kirkland 2010)) and (ii) integration along the z-axes through only one slice with 3D atomic potentials calculated using Quantum Espresso code with PBE-GGA functionals. **b**: Comparison of beam intensity profiles simulated with projected atomic potentials calculated using Quantum Espresso code with PBE-GGA functionals with different slicing, including sub-atomic slicing (0.5 and 0.2 Å slice thicknesses).

APPENDIX C: PROJECTED ATOMIC POTENTIALS AND SUB-ATOMIC SLICING

In the TEMSIM *multislice* code (Kirkland, 2010) the scattering atoms of the specimen are modeled as 2D projected atomic potentials that are calculated from parametrized electron scattering factors of atoms (using the Hartree–Fock approximation), equivalent to integrating the 3D electrostatic potentials of individual atoms along the z-axis from $-\infty$ to $+\infty$. Here, we test the validity of this infinite z-projection method by comparing the results of beam propagation simulations in a crystal using this simple model with results from a more accurate model. For the more accurate model, 3D charge densities of atoms were calculated using the density functional theory (DFT)-based Quantum Espresso code (Giannozzi et al., 2009) with Perdew–Burke–Ernzerhof-generalized gradient approximation (PBE-GGA) functionals (Perdew et al., 1996) and then inverted to 3D electrostatic potentials using an fast Fourier transform (FFT)-based solution of Poisson's equation (Ewald, 1921). The potential could then be sampled with sub-atomic slicing, the projected sub-atomic potentials being calculated by integrating only over the corresponding sub-atomic slice thickness. The results are shown in Figure A.3. Here, for $E_o = 100$ keV and $\alpha_{obj} = 25$ mrad, aberration-free STEM probe intensity profiles were calculated in an isolated column of Ge with interatomic spacing 0.2 nm but with various slice thicknesses. The results show that simple and more accurate models produce very similar beam behavior as the beam travels through an atomic column. The very small discrepancies are due to differences in the bandwidth-limiting schemes of the two different models, resulting in slightly sharper peaks in the projected potential for the PBE-GGA-based model.